Prediction of the photovoltaic performance of the lead-free layered Ruddlesden-Popper organic-inorganic perovskite $(CH_3NH_3)_2GeI_4$

K. Ouassoul, A. El Kenz, and M. Loulidi

Mohammed V University in Rabat, Faculty of Science,
Condensed Matter Laboratory and Interdisciplinary Sciences, Rabat, Morocco.
e-mail: ouassoulkhaoula@gmail.com

A. Benyoussef

Hassan II Academy of Sciences and Techniques, Rabat, Morocco.

M. Azzouz

Al Akhawayn University, School of Science and Engineering,
P.O Box 104, Hassan II Avenue, 53000 Ifrane, Morocco.

Received 10 November 2023; accepted 7 March 2024

Using the density functional theory (DFT) and the spectral limited maximum efficiency (SLME) model, we thoroughly evaluate the material MA_2GeI_4 as a prospective absorber for photovoltaic applications. This material belongs to the family of layered material organic-inorganic Ruddlesden-Popper perovskites, which have attracted interest due to their stability. Our first-principles calculations show that MA_2GeI_4 has a direct bandgap that is suitable for light absorption at 1.37 eV. To understand the source of its exceptional optical properties, the electronic structure, density of states, and optical properties were examined. Also, we used the SLME model to estimate the MA_2GeI_4 solar cell efficiency. The latter was found to be about 32.6% power conversion efficiency. The material's excellent absorption and promising photovoltaic properties contribute to its high efficiency, even when quantum confinement occurs between layers. We found that MA_2GeI_4 is a potential absorber material for solar applications, demonstrating both good absorption characteristics and advantageous electrical properties. This discovery lays the path for additional experimental investigation of MA_2GeI_4 based solar cell.

Keywords: Hybrid perovskite; ruddlesden-popper; DFT; quantum espresso; SLME; photovoltaic performance.

DOI: https://doi.org/10.31349/RevMexFis.70.040502

1. Introduction

Three dimensional (3D) organic-inorganic hybrid perovskites have drawn significant interest in the last decade as materials for solar cells [1]. Their outstanding photovoltaic performance is due to their long diffusion's lengths, high absorption, and low-cost manufacturing [2]. However, the application of these materials in solar cells is limited by the short-term stability due to several reasons, including the hydrophilic nature [3]. Moreover, because of their extreme sensitivity to moisture and temperature, they are rapidly damaged in ambient conditions [4,5]. Many methods have been proposed to increase the 3D halide perovskite stability, such as regulating the boundaries of grain [6], using hydrophobic and stable holes' transporter layers (HTLs) and electrons' transport layers (ETLs) [7,8], adopting the encapsulation [9], and reducing the perovskite dimensionality [10]. The use of two-dimensional (2D) perovskite solar structures (PSKs) is a crucial approach that has received a lot of attention due to their greater stability. 2D PSKs have been shown as better options for photo-stable and moisture-resistant light absorbers [11]. The most viable method to effectively replace the conventional 3D halide perovskites is to use 2D layered Ruddlesden-Popper perovskite [12]. These types of material have a structural formula of $(R)_2(CH_3NH_3)_{n-1}M_nX_{3n+1}$, where the primary aliphatic or aromatic alkylammonium cation is presented by R, M is a divalent metal, X is a halide anion [13], and n could vary from one to infinity, when n is equal to infinity that means that the structure is equivalent to cubic perovskite compounds like $MAPbI_3$ (MA= CH_3NH_3) [14]. The inorganic octahedra in these structures can be linked to one another along the xy plane, but they are kept apart from one another along the z axis by A-site long-chain organic cations. The organic insulating layers serve as potential barriers, while the inorganic semiconducting layers act as potential wells [15]. Thus, these substances have a distinctive layered structure that divides the organic cations from the inorganic perovskite layers to create several quantum wells. Their photovoltaic characteristics are strongly influenced by quantum confinement.

Furthermore, It was confirmed that the layered material MA_2PbI_4 crystalline film has been synthesized successfully using vapor-fumigation technology, and it shows more stability than the three-dimensional absorber $MAPbI_3$ [16]. Also, the thermodynamic and structural stability of this material have been demonstrated theoretically [17]. In this regard, there have been several experimental studies done to create environmentally friendly lead-free materials by replacing the divalent Sn in the place of Pb [18,19]. Earlier first principles calculation investigations have been conducted [20-

23]. These studies investigated the properties of 2D hybrid perovskites based on tin and germanium. The structural and optical properties of the layered perovskite $(BA)_2GeI_4$ (BA = $C_4H_9NH_3$, butylammonium ion) [24] and the 2D $(PEA)_2GeI_4$ where PEA is $C_6H_5(CH_2)_2NH_3$ [25] have been investigated, demonstrating the potential of incorporating germanium into perovskites for solar cell applications. It has been reported that the 2D $(PEA)_2(MA)_{n-1}Pb_nI_{3n+1}$ perovskite with lower n values exhibited remarkable stability against moisture. However, it displayed lower power conversion efficiency (PCE) in comparison with perovskites possessing greater values of n [26].

In this work, using the DFT, we investigated the structural, electronic, and optical properties of the lead-free layered Ruddlesden-Popper organic-inorganic hybrid perovskite MA_2GeI_4 (MA refers to CH_3NH_3). In this structure, $n = 1$, and the conventional PEA is replaced by MA, while Pb is replaced by Ge. We specifically analyzed the bandgap energy and the participation of each atom in the formation of distinct bands in the density of states, closely examining the electronic attributes in relation to their electronic band structure. We also assessed optical properties such as the dielectric function, absorption, refractive index, reflectivity, and extinction coefficient. All these properties were evaluated along different directions of the cell x, y, and z. Subsequently, we determined the efficiency using the SLME model using the results from the first principles' calculations.

2. Materials and methodology

2.1. DFT calculations

Based on the DFT, we study the tetragonal structure of the material $(CH_3NH_3)2GeI_4$ (Fig. 1), which belongs in the tl14 space group.

The material studied in this work is considered to be a 2D bulk perovskite. The introduction of the cations MA which are the shorter chain between the inorganic bilayers results in a reduction of the interlayer space to 9.67 Å, compared to 13.39 Å in BA_2PbI_4 [16].

Calculations were carried out utilizing Quantum Espresso software [27]. The interactions between electrons and ions were characterized through the Projector Augmented Wave (PAW) pseudopotential [28], and the electron-electron exchange-correlation functional was managed with the Generalized Gradient Approximation (GGA), as parameterized by Perdew-Burke-Ernzerhof (PBE). We used the Monkhorst Pack k-mesh grid of $8 \times 8 \times 1$ in our calculations [29].

A substantial body of theoretical work highlights the significance of van der Waals (vdW) interactions in hybrid perovskite materials, particularly in terms of geometry optimization [30-33]. When these dispersive forces are taken into account, the resulting system parameters align closely with experimental values.

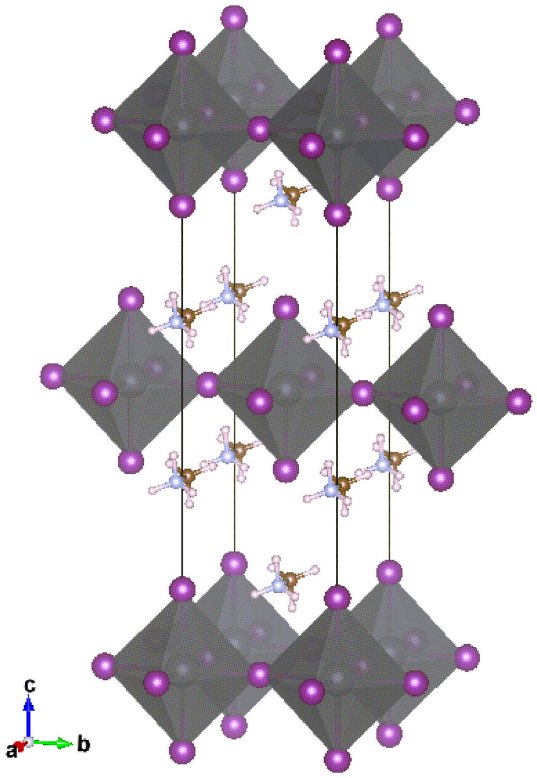

FIGURE 1. The unit cell of the structure MA_2GeI_4.

In the vdW-DF approach, the formula for exchange-correlation energy is presented as follows [30]:

$$E_{XC} = E_X^{\text{GGA}} + E_C^{\text{LDA}} + E_C^{\text{nl}}, \tag{1}$$

where E_X^{GGA} represents the pure exchange energy as determined by the generalized gradient approximation (GGA), and the correlation energy is the total of the local density approximation (LDA) correlation energy E_C^{LDA}, and the non-local electron correlation energy E_C^{nl}.

The exchange functional is written as a function of the enhancement factor $F(s)$, where the exchange energy of a system with density $n(\mathbf{r})$ is given by [66]:

$$E_x^{\text{GGA}}[n(\mathbf{r}), \nabla n(\mathbf{r})] = A_x \int d^3r\, n^{4/3}(\mathbf{r}) F_x^{\text{GGA}}(s), \tag{2}$$

with $A_x = -(3/4)\,(3/\pi)^{1/3}$, $s = |\nabla n|/2k_F n$ is the density gradient, and $k_F \equiv \left(3\pi^2 n\right)^{1/3}$ is the local Fermi wavevector. The exchange enhancement factor (F_x) affects the position of the repulsive Pauli wall for small reduced density gradients. Steeply increasing F_x makes functionals more repulsive and results in longer lattice constants. Considerable efforts have been made to enhance the van der Waals (vdW) functionals by modifying the factor F_x [64]. In our work, we used the vdW-DF-ob86 method, which has been previously demonstrated to be effective in perovskite calculations. The form of the vdW-DF-ob86 exchange factor is given by [64]:

$$F_x = 1 + \frac{\mu s^2}{(1+\mu s^2)^{4/5}}, \quad \mu = 0.1234. \tag{3}$$

So, using this type of functional is the most appropriate for describing the van der Waals in our system. For ionic minimization, there are two convergence thresholds: one on total energy and the other on the forces. In our calculation, the relaxation was deemed complete when the changes in total energy between two consecutive self-consistent field steps were less than 10^{-5} Ry, and the forces on atoms were less than 0.01 eV/Å. We adopted the Broyden-Fletcher-Goldfarb-Shanno (BFGS) method for optimizing atomic positions by minimizing the forces calculated on each atom along the three axes. These forces are a composite of various contributions: non-local, ionic, local, core correction, Hubbard, and a correction term for incomplete self-consistency [65]. In our approach, we did not impose any constraints on the system. We used full structural relaxation, allowing both volume and atomic positions to relax. We used 50 Ry as the energy cutoff to depict the wave functions.

We used the Bolztrap code to calculate the electrical conductivity [34]. The conductivity tensor is given by

$$\sigma_{\alpha,\beta}(i,k) = e^2 \tau_{i,k} \nu_\alpha(i,k) \nu_\beta(i,k), \tag{4}$$

where ν_α is the α component of a charge carrier's group velocity in the i-th band and $\tau_{i,k}$ is the relaxation time of charge carriers:

$$\nu_\alpha(i,k) = \frac{1}{\hbar} \frac{\partial \epsilon_{i,k}}{\partial k_\alpha}. \tag{5}$$

By integrating $\sigma_{\alpha,\beta}(i,k)$, we can obtained The conductivity as a function of the temperature T and the chemical potential μ:

$$\sigma_{\alpha,\beta}(T,\mu) = \sum_i \int \frac{dk}{8\pi^3} \Big[-\frac{\partial f(T,\nu)}{\partial \epsilon} \Big] \sigma_{\alpha,\beta}(i,k). \tag{6}$$

Here, e stands for the electronic charge, $\epsilon_{i,k}$ represents the eigenenergy with wave vector k, and f is the Fermi-Dirac distribution.

2.2. SLME and Sholckley Quiesser methods

In order to calculate the photovoltaic properties of the solar cell at the temperature of $T_c = 300$ K of the absorber $(CH_3NH_3)_2GeI_4$, we adopted the spectroscopic limited maximum efficiency (SLME) method introduced by Yu and Zunger in 2012 [35], and also the Shockley-Quiesser model is used for comparison purposes [36]. According to the American Society for Testing and Materials (ASTM International Standard) [37], which defined the sun spectrum on earth, there are two terrestrial spectral irradiance distributions, namely the direct normal and hemispherical on 37°C tilted surface abbreviated as AM 1.5 D and AM 1.5 G respectively [38]. In this work, we adopted the standard AM 1.5 G solar spectrum (Isun(E)).

The power conversion efficiency of a solar cell η is a measure of how effectively the cell converts the energy of the sun's photons into usable electrical energy. It is typically expressed as a percentage of the total solar energy incident on the cell that is converted into usable electrical energy. η is given by

$$\eta = P_m / P_{in}, \tag{7}$$

where $P_{in} = 1000.37$ W/m^2 is the density of the total incident solar energy [39], and P_m is the density of the maximum output power. The power of a solar cell reaches its maximum at the combination of the maximum current density J_m and voltage V_m.

$$P_m = V_m J_m. \tag{8}$$

Usually, in experiment, the maximum power of a solar cell is characterized by the parameters the short-circuit current density J_{sc} and the open circuit voltage V_{oc} since they are easier to measure than J_m and V_m. Where J_{sc} is defined as the amount of current that passes through the external circuit when the solar cell's electrodes are shorted, and V_{oc} is the voltage that is present across the cell when no current is flowing through it.

The fill factor is the parameter that describes the amount of filling of the J_{sc}-V_{oc} rectangle by the J_m-V_m rectangle [40]

$$FF = \frac{J_m V_m}{J_{sc} V_{oc}}. \tag{9}$$

The current density J and voltage V of the solar cell are related by the following equation [41]:

$$J = J_{sc} - J_0 (e^{(eV/K_B T)} - 1), \tag{10}$$

where e is the electron's charge, T is the temperature, K_B is Boltzmann's constant, J_0 is the reverse saturation current, and J_{sc} is the short-circuit current density, which is

$$J_{sc} = \int_0^\infty a(E) I_{\text{sun}}(E) dE. \tag{11}$$

The reverse saturation current is

$$J_0 = \frac{q\pi}{f_r} \int_0^\infty a(E) I_{bb}(E) dE, \tag{12}$$

where I_{bb} represents the black body spectrum and f_r is the fraction of the radiative recombination current.

$$f_r = e^{(E_g^{da} - E_g)/K_B T_c}, \tag{13}$$

where E_g is the fundamental bandgap and E_g^{da} is the optical gap. The absorptivity $a(E)$ in the SLME model is taken as depending on the geometric factor, *i.e.* the nature of the reflector: if it's a perfect anti-reflective coating then $f_g = 1$, and if it's a reflective back surface then $f_g = 2$

$$a(E) = 1 - e^{(-2\alpha(E)L)} \quad \text{for} \quad f_g = 1, \tag{14}$$

$$a(E) = 1 - e^{(\alpha(E)L)} \quad \text{for} \quad f_g = 2, \tag{15}$$

where $\alpha(E)$ is the absorption coefficient obtained from first-principles calculations. It is, calculated from first principles output and L is the thickness. The SLME can be thus used to study the thickness dependence of the efficiency. The open-circuit voltage V_{oc} of a solar cell is defined as:

$$V_{oc} = \frac{K_B T_c}{e} \ln\left(1 + \frac{J_{sc}}{J_0}\right). \tag{16}$$

Besides, we used the Shockley-Quiesser (SQ) model, which is a theoretical model used to describe the efficiency of a solar cell. It was developed by William Shockley and Hans Queisser in 1961 [36]. It describes the maximum theoretical efficiency of a solar cell, known as the "Shockley-Quiesser limit", which is around 34% for a single-junction solar cell made of a semiconductor with band gap of 1.4 eV. The maximum efficiency of a photovoltaic cell is calculated under the assumption that all photons with an energy above the band gap were absorbed [42]. This means that $a(E)$ should be fixed to unity for $E \geq E_g$ and to zero for $E < E_g$. The process of recombination that the Shockley Quiesser model takes into account is radiative recombination only.

The SQ limit has been used as a guideline to measure the top performance and efficiency of solar cells [42]. Scientists have used this limit to compare different solar cells' performance. There have been significant research efforts to increase solar cell efficiency, but the best ones are still significantly lower than the maximum SQ efficiency of 34% corresponding to the gap energy of 1.4 eV. However, due to its efficiency overestimation, its value can't be achieved in reality. The light absorber in this model has an infinite thickness, and it is considered a perfect blackbody, which means that the absorber presents zero light reflection, refractive index equal to unity, and extinction coefficient equal to zero. This is not the case for standard absorbed that show a refractive index equal to 3 or 4 with an extinction coefficient greater than zero.

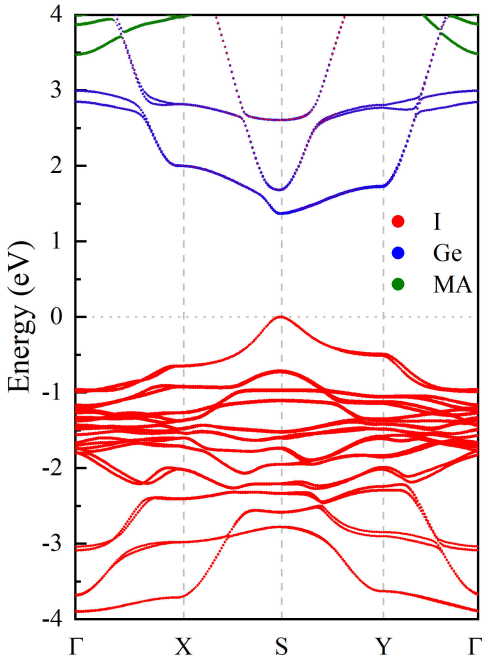

FIGURE 2. Band structure of the structure MA_2GeI_4. MA (green), Ge (blue), and I (red).

3. Results and discussion

3.1. Electronic properties

The band structure of MA_2GeI_4 that is displayed in Fig. 2 is in good agreement with the band structure reported in Ref. [43]. The relative contributions of Ge, I, and MA are indicated by blue, red, and green colors respectively. We observe that the valence band is largely the consequence of I atoms' contribution, while the conduction band is primarily dominated by the Ge contribution. It is obvious that the band gap between the valence band maximum (VBM) and conduction band minimum (CBM) is direct and situated at the S k-point.

To better understand the origin of the states in the conduction and valence bands, we plotted the density of states (DOS) and partial DOS of this 2D perovskite MA_2GeI_4, Fig. 3. The influence of MA molecules on the Density of States (DOS) is primarily situated at a distance from the band edges, suggesting that these MA organic molecules don't directly affect the band gaps of layered perovskites, similar to various other forms of organic-inorganic perovskite [44].

Figure 3 demonstrates the predominance of Ge 4p states in the conduction band and I 5p states in the valence band, consistent with the band contributions shown in Fig. 2. This can also be observed in Fig. 2 through the charge densities of the material in the S k-point for CBM and VBM.

3.2. Binding energy and effective mass

We calculated the effective mass for electrons m_e and holes m_h using the fitting of the calculated band structure near the edges of the conduction and valence bands using the equation:

$$m^* = \left[\hbar^2 \frac{\partial^2 E(k)}{\partial k^2}\right]^{-1}. \tag{17}$$

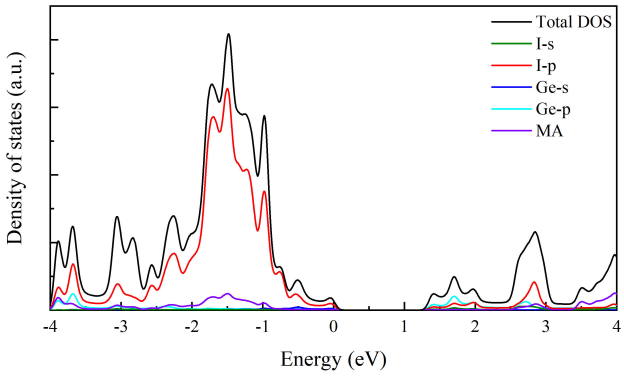

FIGURE 3. Density of states of MA_2GeI_4.

TABLE I. Lattice coordinates, space group, band gap E_g, effective mass of electrons m_e and holes m_h, and binding energy E_b.

	Lattice coordinates			space group	E_g	$m_e(m_0)$	$m_h(m_0)$	E_b(meV)
	a	b	c					
Our work	6.01	5.92	18.69	tl14	1.37(VDW)	0.21	0.15	56.031
Ref. [43]	5.94	5.87	20.11	tl14	1.21(GGA) 1.66(HSE)	0.11	0.11	35.22

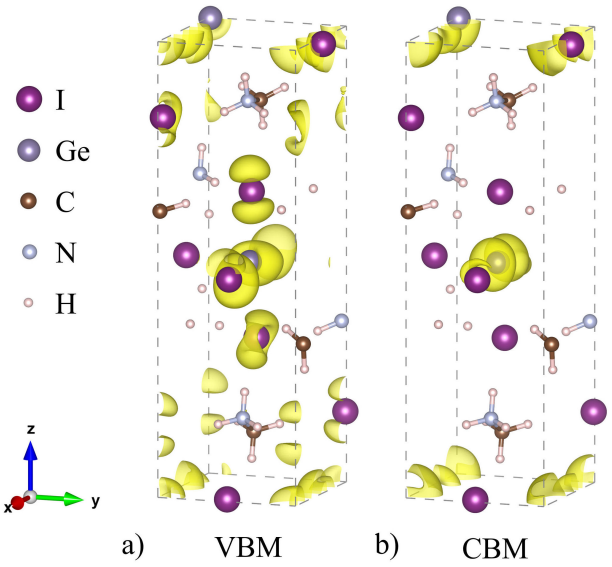

FIGURE 4. Density of charge of MA_2GeI_4 at the S k-point, a) VBM and b) CBM.

We find that $m_e = 0.21$ and $m_h = 0.15$, these values are slightly different from other work [43] due to the difference in the approaches used in our calculations (the code and the absence of hybrid DFT en our calculation).

The energy required to separate electron-hole pairs is known as the exciton's binding energy, E_b. We used the semi-classical Wannier-Mott theory to estimate E_b [45], with the input parameters, namely, the reduced effective mass which is expressed as a function of the electron effective mass m_e and hole effective mass m_h, $\mu = m_e m_h/(m_e + m_h)$, the relative dielectric constant ϵ_r and R_y is the atomic Rydberg energy. E_b is given by [43]

$$E_b = \frac{\mu R_y}{m_0 \epsilon_r^2}. \tag{18}$$

A smaller exciton binding energy allows for easier separation of the electron and hole, thus enhancing device efficiency.

The binding energy calculated in this work for MA_2GeI_4 is in good agreement with existing work [43], and $E_b = 35$ meV is a suitable value for photovoltaic application. While its value is about 172 meV for MA_2PbI_4 according to Zhu *et al.* [16]. In our model for E_b, we did not take into account the quantum and dielectric confinements which are the principal reasons for the high values of the binding energy. However, the existence of the MA cation, which has a relatively high dielectric constant, leads to a decrease in the binding energy. The use of organic barriers with high dielectric constants results in low dielectric-confined 2D perovskites with improved photo-excited carrier dissociation, increased charge carrier mobility, and lower E_b values [46].

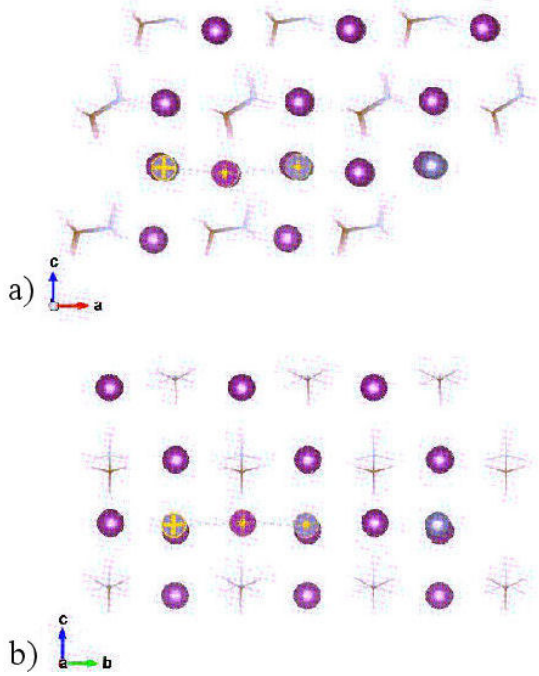

FIGURE 5. Tilting of the octahedra along: (a) x direction and (b) y direction in the structure MA_2GeI_4.

In particular, it has been demonstrated that the binding energy of the 2D perovskites, $(HOCH_2CH_2NH_3)_2PbI_4$ (also known as 2D EA perovskites), possessing an organic component with a high dielectric constant of 37, is only 13 meV. Interestingly, this is 20 times lower than their counterparts 2D-PEA perovskites (PEA, $C_6H_5(CH_2)_2NH_3$), which have a significantly lower dielectric constant of 3.3 for their organic molecule and a binding energy E_b of 250 meV [47].

3.3. The distortion of the octahedra

At the band gap edges, the CBM and VBM are dominated by the inorganic atoms' states. Any small variation in the positions of these atoms could affect the opto-electronic properties of this material. It has been previously shown that the band structure can be changed by changing the identities of halide and metal atoms, but also by controlling the bond an-

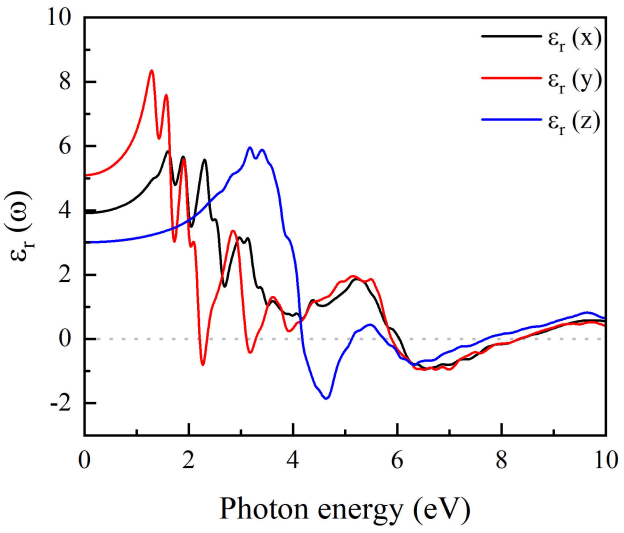

FIGURE 6. Dielectric function' real part.

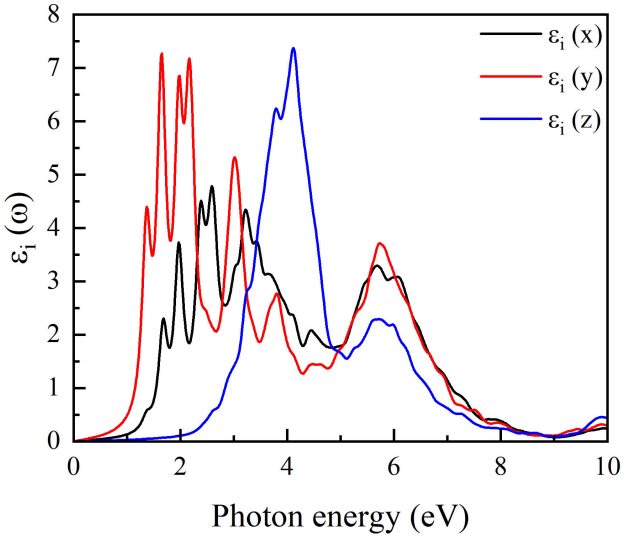

FIGURE 7. Imaginary part of the dielectric function.

gles between these atoms through modifying the size of the organic cation [48]. The tilting of the inorganic part, which is due to the changes in the bond angle, has been mentioned in the known hybrid perovskite $MAPbI_3$ [44,49], and also in the two-dimensional Ruddlesden-Popper perovskites [17].

The tilting angle of the lead halide octahedra (PbX_6) has been identified as an order parameter in lead halide perovskites (LHPs), playing a crucial role in phase transitions. Traditionally, modifications to the perovskite lattice structure have been achieved through static and chemical methods, such as changing the size of the A-site cation to influence the octahedral tilting angle [50,51]. In addition, the bandgap of $CH_3NH_3PbI_3$ at room temperature has been modulated employing ultrafast resonant excitation of the 1 THz phonon in the octahedra PbI_6 [52]. within the same context, recent advancements have shown that through nonlinear THz excitation, it is possible to have a coherent control over the twist modes of the octahedra in order to control the disorder of the dynamic lattice and thus use this application for dynamic charge carrier screening [53].

After the relaxation of our system MA_2GeI_4,we find a lowering in symmetry due to a distortion of the PbI_6 octahedra. As shown in Fig. 6, we calculated the distortion along the x and y dimensions of the unit cell.

The angle Ge$\hat{I}$Ge that characterizes the distortion of the octahedra PbI_6, equal to 169.25°C along x and 170.38°C along y, meaning that the tilting along the x direction is slightly bigger than along the b direction. This result may explain the difference observed in the properties studied in this article between the x and y directions in this material.

4. Optical and transport properties

The transitions between occupied and unoccupied electron states and the way a material reacts to electromagnetic radiation can both be explained by the optical properties. The complex dielectric function explains the nature of the transitions between valence and conduction bands. Using the Kramers-Kroning relation [54,55], we extract the following optical properties: the imaginary and real part of the dielectric function, absorption coefficient, refractive index, and extinction coefficient.

We calculated the real part of the dielectric function, $\epsilon_r(\omega)$. In general,the real part represents the ability of the material to store electric energy, which can arise from its interaction with electromagnetic waves [56]. A larger real part of the dielectric function means the material can store more energy.

As seen in Fig. 6, There is a clear anisotropy in the dielectric properties of the system. The static dielectric constant $\epsilon_r(0)$ is highest in the y direction followed by x and z. The same trend is observed in the visible region of photons' energy between 1.63 and 3.26 eV. This can be explained by the high response to the external field for charge carriers along the y-direction and then the x-direction, where the z-direction has the lowest charge carrier response.

$\epsilon(\omega)$ has their maximum values in the visible range of photons' energy with a maximum value of 5.57 for the non-polarized $\epsilon_r(\omega)$, which is comparable to the maximum of the real part of the dielectric function of the famous material $MAPbI_3$, namely 6.5 [57].

The negative values of the real part of the dielectric function, $\epsilon_r(\omega) < 0$, means that the material reacts to the applied electromagnetic field in a way that prevents the propagation of electromagnetic waves within it. This phenomenon is related to the collective oscillations of free electrons in the substance known as plasmons. These particles cause the light to localize at the surface in the c-direction, particularly in the UV range above 4 eV, leading to an increase in absorption as observed in Fig. 8.

The imaginary part of the dielectric function, $\epsilon_i(\omega)$, is crucial for analyzing the photovoltaic performance because it is directly related to the material's absorption of electromag-

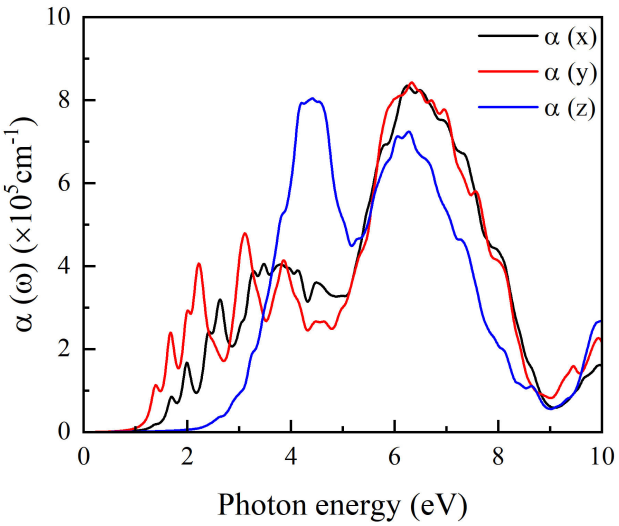

FIGURE 8. Absorption coefficient $\alpha(\omega)$.

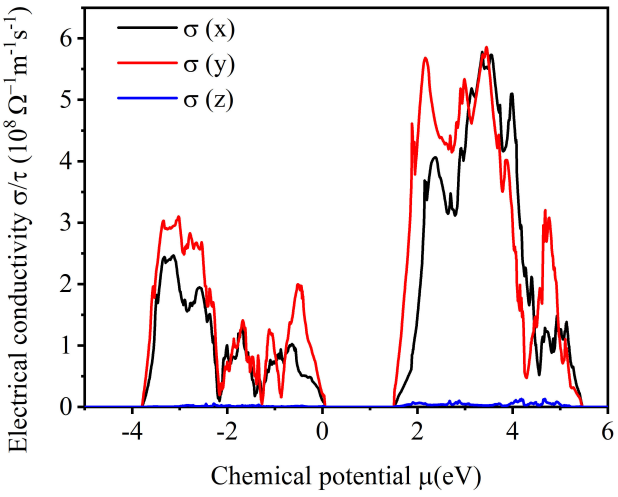

FIGURE 9. Electric conductivity along x, y and z directions of the unit cell.

netic radiation. We calculated this quantity and plotted it in Fig. 7. Higher values are exhibited along the x and y directions, but the imaginary dielectric is practically zero in the c-direction in the visible spectrum region. The principal absorption edge is caused by the direct electrical transition between VBM and CBM, *i.e.* the Ge s-states and Ge p-states, which are the allowed transitions that could be interband in this material according to the rule $\Delta l \pm 0$, with l represents the orbital quantum number, it can be 0, 1, 2, or 3 [58].

Many electronic transitions between occupied and unoccupied states are connected to various peaks. According to Fig. 7, the first exciton peak exists around 1.36 eV, while the second and third peaks are observed at energies 1.65 eV and 1.95 eV, respectively. These peaks are caused by various interband electronic transitions in both direct and indirect bands.

The optical absorption was calculated for different cell directions (Fig. 8). It shows differences in the a and b directions, which are caused by the noncentrosymmetric structure due to the existence of the disordered MA molecules, and also due to the octahedra tilting observed after the relaxation of the system. This tilting has also been shown in the material MA_2PbI_4 [17].

The optical absorption patterns clearly differed from one another in the xy plane and perpendicular to this plane, Fig. 8. We observe that strong optical absorption is present in 2D perovskites in the x and y directions. The maximum value of the absorption in the z direction reaches 1.5×10^5 at 3.18 eV, the edge of the visible region. This value is very low compared to the absorption in the xy plane. The large variation in the dielectric constant between organic MA molecules and inorganic layers also explains the anisotropy of optical absorption.

We also calculated the electric conductivity σ for different directions of the cell and reported it in Fig. 9. Using Boltzmann equation whitin the relaxation time approximation [34].

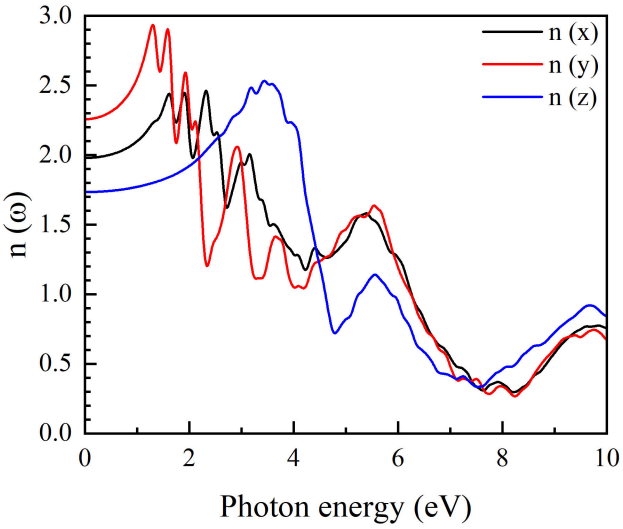

FIGURE 10. Refraction index versus energy.

It is found that σ is much greater in the x and y directions than in the z direction where it is vanishingly small. This is due to the quantum confinement in this type of material, where the organic component acts as a well and barrier to prevent charge carriers from dispersing in the perpendicular direction.

The refractive index $n(\omega)$ is a dimensionless property that explains how light moves through a substance as a function of frequency (ω). It is a measure of its transparency to incident spectral radiation [59].

When an incident electromagnetic wave interacts with a material, the electric field of the wave causes the material's electrons and ions to oscillate. This oscillation generates a microscopic polarization in the material, which affects the way light propagates through the material, the refractive index provides information about this polarisation. Our results as shown in Fig. 10, where we plotted the refractive index as a function of photon energy, are in agreement with the above

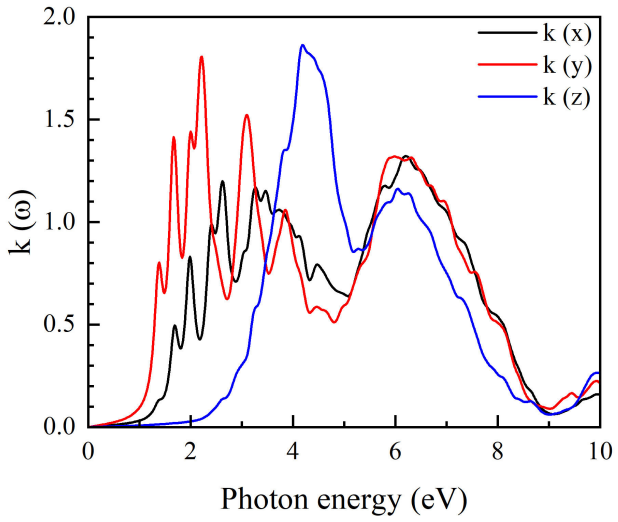

FIGURE 11. The extinction coefficient versus energy.

discussion. The absorption is high (small) for the directions x and y (z-direction) where the refractive index has the largest (lowest) values. the maximum value of the refractive index occurs in the visible range with a value of 2.39 which is in agreement with the refractive index of $MAPbI_3$ which is 2.61 [57].

The calculated coefficient of extinction is shown in Fig. 11. This coefficient is a measurement of how well a substance absorbs electromagnetic radiation. A high extinction coefficient in the in-plane directions means that the material can absorb sunlight more efficiently in those directions. It is further reported that the extinction coefficient decreases with increasing incident photon energy above 6 eV.

5. Photovoltaic performance

We adopted the SLME to calculate the current density and the power density as a function of the voltage. Let J_{sc} and V_{oc} the physical quantities corresponding to the short-circuit current density and the open circuit voltage respectively, while

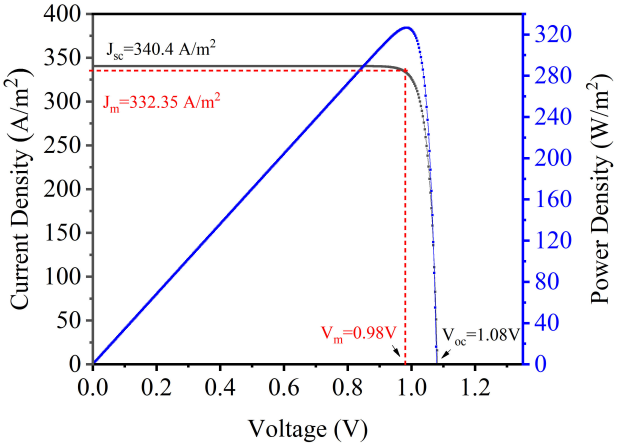

FIGURE 12. The Current density (black curve) and power density (blue curve) are plotted as a function of voltage.

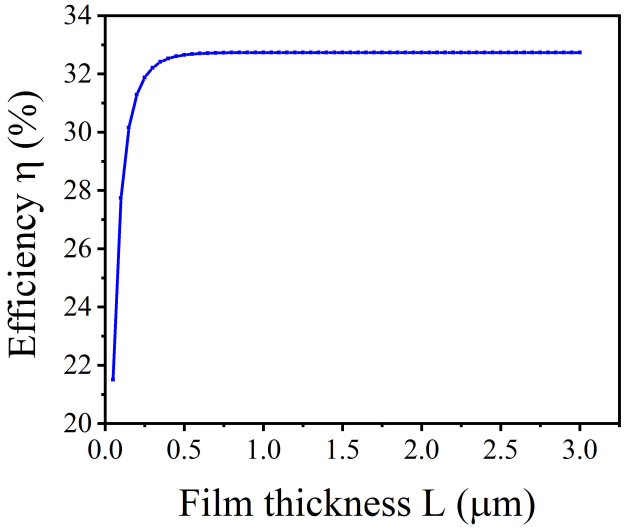

FIGURE 13. Efficiency as a function of the film thickness.

TABLE II. The key J-V parameters of MA_2GeI_4 compared with those studied: experimentally of MA_2PbI_4, using SLME model for $MAPbI_3$, and using Shockley Quiesser SQ model.

Material	J_{sc} (Am^{-2})	V_{oc} (V)	FF	PCE (%)
MA_2GeI_4(SLME)	340.4	1.08	0.88	32.6
MA_2PbI_4(experimental) [16]	210	1.06	0.76	16.92
$MAPbI_3$(SLME) [63]	295	1.16	0.89	31
SQ (Eg=1.4eV) [42]	328.8	1.122	0.89	32.91%

the J_m and V_m are identified from the maximum point of the power density as shown in Fig. 12. A significant current density J_{sc} of 340.4 A/m^2 is shown in the J-V figure and an important value of V_{oc} of 1.08 V. Those values explain the greater values of the output power, fill factor, and efficiency. The ohmic loss, loss of nonradiative recombination, and optical loss are the factors responsible for the differences between the experimental values and our values [41]. Moreover, a small difference between J_m and J_{sc} indicates less non-radiative electron-hole recombination loss. The key $J-V$ parameters of MA_2GeI_4, the fill factor, open circuit voltage, and the short-circuit current density are displayed in the Table II.

Another factor that significantly affects the performance of thin film solar cells is the thickness of the absorbing layer. The efficiency dependence of the thickness is plotted in Fig. 13. Lower PCE values result from excessively low thickness because of the extremely low light absorption. The PCE is enhanced by the increased light absorption as the absorbing thickness is increased tending to the Shockley-Queisser limit of this material. The PCE of the cell is unchanged by thickness values greater than 500 nm. However, The PCE values become saturated as thickness increases because of greater recombination rates (depending on the diffusion length), which means that when the thickness increases,

the distance that charge carriers must travel to get the appropriate electrodes increases. This longer path increases the probability of recombination losses, where electrons and holes recombine before they can be collected. It is important to study the effect of the thickness because the reduced material requirements for thinner absorbing layers might result in lower manufacturing costs [61,62]. The PCE predicted for $MAPbI_3$ using the SLME method reached the value of 31% according to Sha *et al.* [63].

6. Conclusion

In this study, we used the Density Functional Theory (DFT) to rigorously compute the structural, electronic, and optical properties of the lead-free two-dimensional (2D) Ruddlesden-Popper organic-inorganic hybrid perovskite $(CH_3NH_3)_2GeI_4$. Our results highlight the promising potential of this material for photovoltaic solar cell applications. Because of its direct band gap with an optimal value of 1.37 eV, the spectrum of photoconductivity, low effective mass for both electrons and holes, low binding energy, and the high absorption coefficient make it a promising material in the field of photovoltaic. We compared the maximum of the real part of the dielectric function, the absorption, and the maximum value of the refractive index with those of the known material $MAPbI_3$ and found similar values.

In this work, we delved into the anisotropic variations observed in the physical properties of the material across different cell orientations. This anisotropy is multifaceted; it stems from the presence of the organic molecule, the differential distortion of the inorganic octahedra, and distinct dielectric properties. More specifically, variations in the a and b directions are primarily influenced by the organic molecule and the distortion of the inorganic octahedra. In contrast, in the c-direction, the differences predominantly arise from the contrasting dielectric properties between the organic and inorganic sections of the material.

We used the Spectroscopic Limited Maximum Efficiency to calculate the photovoltaic performance of $(CH_3NH_3)_2GeI_4$. J_{sc}, V_{oc}, FF, and PCE were calculated and compared with the experimental values of the material MA_2PbI_4 and with the theoretical values using the same SLME method for the material $MAPbI_3$. This comparison confirms the promising potential of this material in the field of photovoltaics and solar cells.

1. S. Meloni *et al*., Ionic polarization-induced current–voltage hysteresis in ch3nh3pbx3 perovskite solar cells. *Nature communications*, **7** (2016) 10334, https://doi.org/10.1038/ncomms10334
2. M. A. Green, A. Ho-Baillie, and H. J. Snaith, The emergence of perovskite solar cells. *Nature photonics*, **8** (2014) 506, https://doi.org/10.1038/nphoton.2014.134
3. C. Ma *et al.*, 2d/3d perovskite hybrids as moisture-tolerant and efficient light absorbers for solar cells. *Nanoscale*, **8** (2016) 18309, https://doi.org/10.1039/C6NR04741F
4. B. Feng, J. Duan, L. Tao, J. Zhang, and H. Wang, Enhanced performance in perovskite solar cells via bromide ion substitution and ethanol treatment. *Applied Surface Science* **430** (2018) 603, https://doi.org/10.1016/j.apsusc.2017.06.064
5. E. Bi *et al*., Diffusion engineering of ions and charge carriers for stable efficient perovskite solar cells. *Nature communications*, **8** (2017) 15330, https://doi.org/10.1038/ncomms15330
6. Z. Meng, D. Guo, J. Yu, and K. Fan. Investigation of al2o3 and zro2 spacer layers for fully printable and hole-conductor-free mesoscopic perovskite solar cells. *Applied Surface Science*, **430** (2018) 632, https://doi.org/10.1016/j.apsusc.2017.05.018
7. B. Abdollahi Nejand, V. Ahmadi, S. Gharibzadeh, and H. Reza Shahverdi, Cuprous oxide as a potential low-cost hole-transport material for stable perovskite solar cells. *ChemSusChem*, **9** (2016) 302, https://doi.org/10.1002/cssc.201501273
8. C. Liu *et al.*, High-efficiency and uv-stable planar perovskite solar cells using a low-temperature, solution-processed electron-transport layer. *ChemSusChem*, **11** (2018) 1232, https://doi.org/10.1002/cssc.201702248
9. F. Matteocci *et al*., Encapsulation for long-term stability enhancement of perovskite solar cells. *Nano Energy*, **30** (2016) 162, https://doi.org/10.1016/j.nanoen.2016.09.041
10. F. Arabpour Roghabadi *et al*., Stability progress of perovskite solar cells dependent on the crystalline structure: From 3d abx 3 to 2d ruddlesden–popper perovskite absorbers. *J. Mat. Chem. A*, **7** (2019) 5898, https://doi.org/10.1039/C8TA10444A
11. C. Lan, Z. Zhou, R. Wei, and J. C. Ho, Two-dimensional perovskite materials: from synthesis to energy-related applications. *Materials today energy* **11** (2019) 61, https://doi.org/10.1016/j.mtener.2018.10.008
12. Y. Chen, Y. Sun, J. Peng, J. Tang, K. Zheng, and Z. Liang, 2d ruddlesden–popper perovskites for optoelectronics. *Advanced Materials*, **30** (2018) 1703487 https://doi.org/10.1002/adma.201703487
13. D. H. Cao, C. C. Stoumpos, O. K. Farha, J. T. Hupp, and M. G. Kanatzidis, 2d homologous perovskites as light-absorbing materials for solar cell applications. *Journal of the American Chemical Society*, **137** (2015) 7843, https://doi.org/10.1021/jacs.5b03796
14. E. T. McClure, A. P. McCormick, and P. M. Woodward, Four lead-free layered double perovskites with the n= 1 ruddlesden–popper structure. *Inorganic Chemistry*,

59 (2020) 6010, https://doi.org/10.1021/acs.inorgchem.0c00009

15. X. Hong, T. Ishihara, and A.V. Nurmikko, Dielectric confinement effect on excitons in pbi 4-based layered semiconductors. *Physical Review B*, **45** (1992) 6961, https://doi.org/10.1103/PhysRevB.45.6961
16. X. Zhu *et al.*, Vapor-fumigation for record efficiency two-dimensional perovskite solar cells with superior stability. *Energy Environ. Sci.* **11** (2018) 3349, https://doi.org/10.1039/C8EE02284D
17. Y. Li, *First-Principles Study of Hybrid Halide Perovskites and Beyond for Optoelectronic Applications*. (University of California, San Diego, 2020).
18. D. H Cao *et al.*, Thin films and solar cells based on semiconducting two-dimensional ruddlesden–popper (ch3 (ch2) 3nh3) 2 (ch3nh3) n- 1sn n i3 n+ 1 perovskites. *ACS Energy Letters*, **2** (2017) 982, https://doi.org/10.1021/acsenergylett.7b00202
19. K. P. Marshall, R. I. Walton, and R. A. Hatton, Tin perovskite/fullerene planar layer photovoltaics: improving the efficiency and stability of lead-free devices. *Journal of materials chemistry A*, **3** (2015) 11631, https://doi.org/10.1039/C5TA02950C
20. L. Ma, M.-Gang Ju, J. Dai, and X. Cheng Zeng, Tin and germanium based two-dimensional ruddlesden–popper hybrid perovskites for potential lead-free photovoltaic and photoelectronic applications. *Nanoscale*, **10** (2018) 11314, https://doi.org/10.1039/C8NR03589J
21. Z. Wang, A. M. Ganose, C. Niu, and D. O. Scanlon, First-principles insights into tin-based two-dimensional hybrid halide perovskites for photovoltaics. *Journal of Materials Chemistry A*, **6** (2018) 5652, https://doi.org/10.1039/C8TA00751A
22. L. Wu, P. Lu, Y. Li, Y. Sun, J. Wong, and K. Yang, First-principles characterization of two-dimensional (ch 3 (ch 2) 3 nh 3) 2 (ch 3 nh 3) n- 1 ge n i 3n+ 1 perovskite. *Journal of Materials Chemistry A*, **6** (2018) 24389, https://doi.org/10.1039/C8TA10055A
23. I. U. l. Haq, G. Rehman, H. A. Yakout, and I. Khan, Structural and optoelectronic properties of ge- and si -based inorganic two dimensional ruddlesden popper halide perovskites. *Materials Today Communications*, **33** (2022) 104368, https://doi.org/10.1016/j.mtcomm.2022.104368
24. D. B Mitzi, Synthesis, crystal structure, and optical and thermal properties of (c4h9nh3) 2mi4 (m= ge, sn, pb). *Chemistry of materials*, **8** (1996) 791, https://doi.org/10.1021/cm9505097
25. P. Cheng *et al.*, (c6h5c2h4nh3) 2gei4: a layered two-dimensional perovskite with potential for photovoltaic applications. *The journal of physical chemistry letters*, **8** (2017) 4402, https://doi.org/10.1021/acs.jpclett.7b01985
26. B. R. Sutherland and E. H. Sargent, Perovskite photonic sources. *Nature Photonics*, **10** (2016) 295, https://doi.org/10.1038/nphoton.2016.62
27. P. Giannozzi *et al.*, Quantum espresso: a modular and open-source software project for quantum simulations of materials. *Journal of physics: Condensed matter*, **21** (2009) 395502, https://doi.org/10.1088/0953-8984/21/39/395502
28. P. E. Blöchl. Projector augmented-wave method. *Physical review B*, **50** (1994) 17953, https://doi.org/10.1103/PhysRevB.50.17953
29. D.J. Chadi, Special points for brillouin-zone integrations. *Physical Review B*, **16** (1977) 1746, https://doi.org/10.1103/PhysRevB.16.1746
30. M. Dion, H. Rydberg, E. Schröder, D. C. Langreth, and B. I. Lundqvist, Van der waals density functional for general geometries. *Physical review letters*, **92** (2004) 246401, https://doi.org/10.1103/PhysRevLett.92.246401
31. T. Thonhauser *et al.*, Van der waals density functional: Self-consistent potential and the nature of the van der waals bond. *Physical Review B*, **76** (2007) 125112, https://doi.org/10.1103/PhysRevB.76.125112
32. G. Román-Pérez and J. M. Soler, Efficient implementation of a van der waals density functional: application to double-wall carbon nanotubes. *Physical review letters*, **103** (2009) 096102, https://doi.org/10.1103/PhysRevLett.103.096102
33. M. A. Perez-Osorio, A. Champagne, M. Zacharias, G.-M. Rignanese, and F. Giustino, Van der waals interactions and anharmonicity in the lattice vibrations, dielectric constants, effective charges, and infrared spectra of the organic–inorganic halide perovskite ch3nh3pbi3. *The Journal of Physical Chemistry C*, **121** (2017) 18459, https://doi.org/10.1021/acs.jpcc.7b07121
34. G. K. H. Madsen and D. J. Singh, Boltztrap a code for calculating band-structure dependent quantities. *Computer Physics Communications*, **175** (2006) 67, https://doi.org/10.1016/j.cpc.2006.03.007
35. L. Yu and A. Zunger, Identification of potential photovoltaic absorbers based on first-principles spectroscopic screening of materials. *Physical review letters*, **108** (2012) 068701, https://doi.org/10.1103/physrevlett.108.068701
36. W. Shockley and H. J. Queisser, Detailed balance limit of efficiency of p-n junction solar cells. *Journal of applied physics*, **32** (1961) 510, https://doi.org/10.1063/1.1736034
37. ASTM.
38. American Society for Testing, Materials. Committee G03 on Weathering, and Durability. *Standard tables for reference solar spectral irradiances: direct normal and hemispherical on 37Å tilted surface*. (ASTM international, 2003).
39. K. Emery and D. Myers, Reference solar spectral irradiance: air mass 1.5. (*Center, RERD, Ed*, 2009).
40. H. Qu and X. Li, Temperature dependency of the fill factor in pv modules between 6 and 40 c. *Journal of Mechanical Science and Technology*, **33** (2019) 1981, https://doi.org/10.1007/s12206-019-0348-4
41. J. Qian *et al.*, Spectroscopic limited practical efficiency (slpe) model for organometal halide perovskites solar cells evaluation. *Organic Electronics*, **59** (2018) 389, https://doi.org/10.1016/j.orgel.2018.05.056

42. S. Rühle, Tabulated values of the shockley–queisser limit for single junction solar cells. *Solar energy*, **130** (2016) 139, https://doi.org/10.1016/j.solener.2016.02.015

43. Khaoula Ouassoul, Abdallah El Kenz, Mohammed Loulidi, Abdelilah Benyoussef, and Mohamed Azzouz. Effect of orientation of the cation ch3nh3 on exciton's mobility in ch3nh3pbi3. *Chinese Journal of Physics*, **80** (2022) 34, https://doi.org/10.1016/j.cjph.2022.09.018

44. D. Yang *et al.*, Functionality-directed screening of pb-free hybrid organic-inorganic perovskites with desired intrinsic photovoltaic functionalities. *Chemistry of Materials*, **29** (2017) 524, https://doi.org/10.1021/acs.chemmater.6b03221

45. A. O. El-Ballouli, O. M. Bakr, and O. F. Mohammed, Structurally tunable two-dimensional layered perovskites: from confinement and enhanced charge transport to prolonged hot carrier cooling dynamics. *The journal of physical chemistry letters*, **11** (2020) 5705, https://doi.org/10.1021/acs.jpclett.0c00359

46. B. Cheng *et al.*, Extremely reduced dielectric confinement in two-dimensional hybrid perovskites with large polar organics. *Communications Physics*, **1** (2018) 80, 10.1038/s42005-018-0082-8

47. M. R. Filip, G. E. Eperon, H. J. Snaith, and F. Giustino, Steric engineering of metal-halide perovskites with tunable optical band gaps. *Nature communications*, **5** (2014) 5757, https://doi.org/10.1038/ncomms6757

48. K. Korshunova, L. Winterfeld, W. J. D. Beenken, and E. Runge, Thermodynamic stability of mixed pb: Sn methyl-ammonium halide perovskites. *physica status solidi (b)*, **253** (2016) 1907, https://doi.org/10.1002/pssb.201600136

49. P.S. Whitfield *et al.*, Structures, phase transitions and tricritical behavior of the hybrid perovskite methyl ammonium lead iodide. *Scientific reports*, **6** (2016) 35685, https://doi.org/10.1038/srep35685

50. H. Mashiyama *et al.*, Displacive character of the cubic-tetragonal transition in $ch_3nh_3pbx_3$. *Journal of the Korean Physical Society*, **42** (2003) 1026,

51. H. Kim *et al.*, Direct observation of mode-specific phonon-band gap coupling in methylammonium lead halide perovskites. *Nature communications*, **8** (2017) 687, https://doi.org/10.1038/s41467-017-00807-x

52. M. Frenzel *et al.*, Nonlinear thz control of the lead halide perovskite lattice. *arXiv preprint arXiv:2301.03508*, (2023), https://doi.org/10.1126/sciadv.adg3856

53. R de L Kronig. On the theory of dispersion of x-rays. *Josa*, **12** (1926) 547, https://doi.org/10.1364/JOSA.12.000547

54. H. Anthony Kramers, La diffusion de la lumiere par les atomes. In *Atti Cong. Intern. Fisica (Transactions of Volta Centenary Congress) Como*, **2** (1927) 545.

55. R. Mayengbam, A. Srivastava, S.K. Tripathy, and G. Palai, Electronic structure and optical properties of gallium-doped hybrid organic–inorganic lead perovskites from first-principles calculations and spectroscopic limited maximum efficiencies. *The J. Phys. Chem. C*, **123** (2019) 23323, https://doi.org/10.1021/acs.jpcc.9b03835

56. P. Loper *et al.*, Complex refractive index spectra of ch3nh3pbi3 perovskite thin films determined by spectroscopic ellipsometry and spectrophotometry. *The journal of physical chemistry letters*, **6** (2015) 66, https://doi.org/10.1021/jz502471h

57. N. Baaalla, Y. Ammari, E.K. Hlil, R. Masrour, A. El Kenz, and A. Benyoussef, Study of optical, electrical and photovoltaic properties of ch3nh3pbi3 perovskite: ab initio calculations. *Physica Scripta*, **95** (2020) 095104, https://doi.org/10.1088/1402-4896/abae1e

58. N.M. Ravindra, P. Ganapathy, and J. Choi, Energy gap–refractive index relations in semiconductors–an overview. *Infrared physics & technology*, **50** (2007) 21, https://doi.org/10.1016/j.infrared.2006.04.001

59. M. Rai, L. Helena Wong, and L. Etgar, Effect of perovskite thickness on electroluminescence and solar cell conversion efficiency. *The J. Phys. Chem. Lett.*, **11** (2020) 8189, https://doi.org/10.1021/acs.jpclett.0c02363

60. Z. Xiao, Q. Dong, C. Bi, Y. Shao, Y. Yuan, and J. Huang, Solvent annealing of perovskite-induced crystal growth for photovoltaic-device efficiency enhancement. *Advanced Materials*, **26** (2014) 6503, https://doi.org/10.1002/adma.201401685

61. W. E.I. Sha, X. Ren, L. Chen, and W. C.H. Choy, The efficiency limit of ch3nh3pbi3 perovskite solar cells. *Applied Physics Letters*, **106** (2015) 221104, https://doi.org/10.1063/1.4922150

62. J. Klimes, and D. Bowler, and A. Michaelides, Van der Waals density functionals applied to solids. *Bulletin of the American Physical Society*, **56** (2011) 195131, https://doi.org/10.1103/PhysRevB.83.195131

63. J. D. Head, and M. C. Zerner, A Broyden-Fletcher-Goldfarb-Shanno optimization procedure for molecular geometries. *Chemical physics letters*, **122** (1985) 1, https://doi.org/10.1016/0009-2614(85)80574-1

64. E. D. Murray, and K. Lee, and D. C. Langreth, Investigation of exchange energy density functional accuracy for interacting molecules *J. Chem. Theory and Comp.*, **5** (2009) 2754, https://doi.org/10.1021/ct900365q

65. Y. Shao *et al.*, Unlocking surface octahedral tilt in two-dimensional Ruddlesden-Popper perovskites *Nature communications*, **13** (2022) 138, https://doi.org/10.1038/s41467-021-27747-x